Spatial and Temporal Scaling of Unequal Microbubble Coalescence [*]

Rou Chen[1], **Huidan (Whitney) Yu**[†1], **Likun Zhu**[1], **Taehun Lee**[2], and **Raveena M. Patil**[1]

[1]Mechanical Engineering Department, Indiana University-Purdue University, Indianapolis(IUPUI), IN46202, USA

[2]Mechanical Engineering Department,The City College of New York, NY10031,USA

We numerically study coalescence of air microbubbles in water, with density ratio 833 and viscosity ratio 50.5, using lattice Boltzmann method. The focus is on the effects of size inequality of parent bubbles on the interfacial dynamics and coalescence time. Twelve cases, varying the size ratio of large to small parent bubble from 5.33 to 1, are systematically investigated. The "coalescence preference", coalesced bubble closer to the larger parent bubble, is well observed and the captured power-law relation between the preferential relative distance χ and size inequality γ, $\chi \sim \gamma^{-2.079}$, is consistent to the recent experimental observations. Meanwhile, the coalescence time also exhibits power-law scaling as $T \sim \gamma^{-0.7}$, indicating that unequal bubbles coalesce faster than equal bubbles. Such a temporal scaling of coalescence on size inequality is believed to be the first-time observation as the fast coalescence of microbubbles is generally hard to be recorded through laboratory experimentation.

Keywords: microbubble coalescence, coalescence preference, power-law scaling, lattice Boltzmann method, large density ratio

Introduction

Microbubbles have a myriad of applications in food industry, material science, medicine, and pharmacology. Over the last decade, there has been significant progress towards the development of microbubbles as theranostics for a wide variety of biomedical applications. The unique ability of microbubbles to respond to ultrasound makes them useful agents for contrast ultrasound imaging[1–4]. The similar size of a microbubble as that of a red blood cell allows it to display similar rheology in the microvessels and capillaries throughout the body[5], making them good mediators for targeted drug and gene delivery[2,6] and therapies[7,8]. In the environmental industry, the most common application of microbubbles is in the water and waste-water treatment[9–13]. Important micro/nano bubble technologies involved in lab-on-a-chip[14,15], airlift bioreactor[16,17], fluorinations[18], hydrogenation[19,20] and DNA analysis[21] are attracting more and more attention. Bubble coalescence is a common phenomenon in different types of applications as the surface areas when bubbles are in touch tend to minimize. For the purpose to control gas/liquid dynamics, the coalescence in some systems needs to be prevented or suppressed in order to maintain a stable mixing condition between the gas and liquid phase. However in other systems, efficient coalescence might be desirable to enhance

the phase separation process. Therefore, it is essentially important to understand the underlying physics of bubble coalescence for effective control of gas-liquid systems.

There has been a long history of studying the bubble coalescence mechanisms through experiments[22,23] and theoretical modeling[24]. These early research focused on ideal, stagnant, and millimeter-sized bubbles in free spaces. For microbubbles, with their diameters from $1\mu m$ to 1 mm, a recent review[25] provides a comprehensive and systematic collection of the diverse bubble generation methods to satisfy emerging technological, pharmaceutical, and medical demands. However, the delicate and ephemeral nature of microbubble coalescence poses significant technical challenges to the precise quantification. In spite of the few important attempts through experimental[26–28] and radiological measurements[29], the fundamentals of coalescence dynamics associated with hydrodynamics and mass transport, including the temporal/spatial scales, have not been well understood. For example, "coalescence preference" has been a puzzling tendency observed in experimentation[29,30] for the merged bubble to be preferentially located closer to the larger of its two parent bubbles. It has been found that the location of the merged bubble is linked by the parent bubble size ratio with a power-law relationship, but the dynamics to drive such a preference is not addressed.

In this work, we systematically study the coalescence of air microbubbles in water using the lattice Boltzmann method (LBM)[31,32]. The focus is on the effects of size inequality of parent bubbles on the interfacial dynamics and coalescence time. Twelve cases, varying the size ratio of large to small bubbles, γ, from 5.33 to 1, are systematically investigated. The aforementioned coalescence preference phenomenon and its power-law scaling[29,30] are captured. Meanwhile, we discover that the coalescence time from two parent bubbles to one coalesced bubble also has a power-law scaling with the size inequality, showing that larger size inequality causes faster coalescence. To understand the underlying physics behind the spatial and temporal scaling, we explore the coalescing mechanism. The kinetic-based LBM has emerged as an alternative for simulating a broad class of complex flows[33,34]. It is considered as a mesoscopic method, bridging the microscopic molecular motion and their collective behavior represented by hydrodynamic and thermodynamic variables, such as velocity, pressure, and temperature. The main advantage of the LBM is its suitability to mimic the intermolecular interactions at the two-fluid interface and recover the appropriate multi-phase dynamics without demanding computation cost. In the past three decades, several multi-phase models using LBM have been developed, including the color fluid model[35], the pseudo-potential model[36,37], the mean-field model[38,39], the phase-field model[40,41], and the entropic LBM[42]. These methods have been continuously refined and applied to simulate various multi-phase flow problems (see both general LBM reviews[33,34] and specific multi-phase LBM reviews[43,44], and therein references). In spite of efforts and successful applications in various flow systems, simulation of multi-phase flows with large density and viscosity ratios between two fluids, as the current application targets, is still challenging. Numerical instability is critical if there is no proper treatment of the high density gradient across the interface[45]. Such an issue also exists in conventional NS solvers[46]. Among those, the free energy model[38–41,45,47] has been demonstrated to be more suitable for dealing with a large density ratio of

up to 1000[48] between two fluids. Furthermore, this model has the potential to minimize parasitic current, which is a small-amplitude artificial (nonphysical) velocity field arising from an imbalance of discretized force across the interface. Such a parasitic current appears in all the LBM multi-phase models[44]. In the current work, we employ the free-energy modeling approach that was originated by He *et al.*[38,39] based on the free-energy theory[49–51] first introduced by Swift *et al.*[40,41]. This model has been continuously developed and refined in the last 10 years by Lee's group[45,47,52,53], and it has been demonstrated that the parasitic current has been eliminated[47].

Lattice Boltzmann Modeling for Two-fluid Flows

When the flow involves two fluids, the interfacial behavior arises as a result of microscopic long-range interactions among the constituent molecules of the system[54]. As a result, accounting for interfacial dynamics over a broad range of length and time scales is required in the modeling. There exists two critical issues in the modeling of multi-phase flow. First, fluid-fluid interface is a contact discontinuity, where the density is discontinuous but the pressure and velocity are continuous across the interface. Thus, the state equation of ideal gas, used in the LBM modeling for single phase flow, is no longer valid. Non-ideal effects must be introduced through the intermolecular forces between fluids. Second, the numerical instability caused by the density discontinuity across the interface would pose a severe obstacle when the density ratio is large. It has been well understood that a parasitic current introduced by a slight imbalance in the interfacial stresses due to truncation errors is the key to suppressing parasitic current in the modeling of intermolecular forces[44]. Targeting to simulate microbubbles coalescence with a large density ratio of up to 1000, e.g. air bubble in water, we employ the LBM model that has been continuously developed and refined in the last 10 years by Lee's group[45,47,52,53]. The following equations are synthesized from open references[47,53].

Governing equations for diffusive interface

Using a diffuse interface to separate phases is a popular technique in the modeling of multi-phase flow. The advantages include the ease of implementation, even for complex three-dimensional interfaces, and the suitability to capture singular phenomena such as interface rupture, coalescence, or phase change. For a binary flow, the continuity equation for the species i of binary fluids can be written as

$$\partial \tilde{\rho}_i / \partial t + \nabla \cdot \tilde{\rho}_i \mathbf{u}_i = 0, \qquad i = 1, 2 \tag{1}$$

where $\tilde{\rho}_i$ and $\mathbf{u}_i$ denote the local density and velocity of species i. The total density, $\rho (= \tilde{\rho}_1 + \tilde{\rho}_2)$, is conserved in the entire domain. The local density $\tilde{\rho}_i$ and velocity $\mathbf{u}_i$ are linked to the volume averaged velocity $\mathbf{u}$, the bulk density value ρ_i, and the volumetric diffusive flux $\mathbf{j}_i$ of species i (rate of volume flow across a unit area) by

$$\rho_i \mathbf{j}_i = \tilde{\rho}_i (\mathbf{u}_i - \mathbf{u}), \qquad i = 1, 2 \tag{2}$$

If the diffusive flow rate is not related to the densities but instead to the local compositions of two species, $\mathbf{j}_1 = -\mathbf{j}_2 = \mathbf{j}$ can be assumed[46], yielding $\nabla \cdot \mathbf{u} = 0$. Furthermore, if $\mathbf{j}$ is assumed to be proportional to a thermodynamic driving force, i. e. the gradient of the chemical potential μ, as $\mathbf{j} = -M \nabla \mu$ with $M (> 0)$ the mobility[55] and C

$(= \tilde{\rho}_i/\rho_i)$ the composition, Eq. (1) becomes

$$\partial C/\partial t + \mathbf{u} \cdot \nabla C = \nabla \cdot (M\nabla\mu) \tag{3}$$

where μ is the chemical potential defined as

$$\mu = \mu_0 - \kappa\nabla^2 C \tag{4}$$

in which μ_0 is the classical part of the chemical potential. In the vicinity of the critical point, simplification of van der Waals equation of state can be made[54] for the control of interface thickness and surface tension at equilibrium. In this case, we assume that the energy E_0 takes a form[56] of $E_0 = \beta C^2(C-1)^2$ with β being a constant. As a result, $\mu_0 = \partial E_0/\partial C = 2\beta C(C-1)(2C-1))$. The equilibrium profile of C is determined such that the energy E_0 is minimized and reads $\mu = const$ in one dimension. In an interface at equilibrium, the interface profile is

$$C(z) = 0.5 + 0.5\tanh(2z/D) \tag{5}$$

where z is the distance normal to the interface and D is the (numerical) interface thickness, which is chosen based on accuracy and stability. Given D and β, one can compute the gradient parameter $\kappa = \beta D^2/8$ and the surface tension force $\sigma = \sqrt{2\kappa\beta}/6$.

Lattice Boltzmann equations for binary flow

For a binary flow, we introduce the intermolecular force[53]

$$\mathbf{F} = \frac{1}{3}\nabla\rho c^2 - \nabla p_1 - C\nabla\mu \tag{6}$$

where p_1 is the hydrodynamic pressure, whereas the thermodynamic pressure p_0 is defined by $p_0 = C\partial E_0/\partial C - E_0 = \beta C^2(C-1)(3C-1)$. The total pressure is $p = p_0 + p_1 - \kappa C\nabla^2 C + \kappa|\nabla C|^2/2$. When Ma is low, $p_1/p_0 \sim O(Ma^2)$, and all thermodynamic quantities are independent of the hydrodynamic pressure[57], meaning that the density of the fluid does not depend on the hydrodynamic pressure. In the motionless flow, the contribution from the hydrodynamic pressure p_1 disappears, as do parasitic currents.

The primary variable in the LBM is the so called particle distribution function, $f(\mathbf{x}, \xi, t)$, defined as the density weighted probability to find a fluid particle in the molecular phase space, including spatial location $\mathbf{x}$ and molecular velocity ξ at time t. The evolution of this variable is governed by the Boltzmann equation[58]. After the molecular phase space is discretized toward only including a minimal set of molecular velocities (i.e. the microscopic velocity field ξ on unit lattice yields the discrete microscopic velocity $\mathbf{e}_\alpha, \alpha = 0, 1, 2, \cdots, b)$[59], the lattice Boltzmann equation (LBE) (before the time discretization) including the intermolecular force reads[38]

$$\partial f_\alpha/\partial t + \mathbf{e}_\alpha \cdot \nabla f_\alpha = -(f_\alpha - f_\alpha^{eq})/\lambda + \frac{3}{c^2}(\mathbf{e}_\alpha - \mathbf{u}) \cdot \mathbf{F} f_\alpha^{eq} \tag{7}$$

where f_α is the equilibrium particle distribution function with discrete molecular velocity $\mathbf{e}_\alpha$ along the α-th direction and λ is the relaxation time related to the kinematic viscosity $\nu = \frac{1}{3}c^2\lambda$. The equilibrium distribution function is

a function of local macroscopic density and velocity and is usually formulated up to $O(u^2)$

$$f_\alpha^{eq} = \rho\omega_\alpha\Big[1 + \frac{3(\mathbf{e}_\alpha \cdot \mathbf{u})}{c^2} + \frac{9(\mathbf{e}_\alpha \cdot \mathbf{u})^2}{2c^4} - \frac{3u^2}{2c^2}\Big] \tag{8}$$

where ω_α is the weight associated with a particular discretized velocity $\mathbf{e}_\alpha$, ρ and $\mathbf{u}$ are macroscopic density and velocity respectively, and $c = \delta x/\delta t = 1$ in lattice units (i.e., $\delta t = \delta x = 1$).

In the single phase LBM modeling, the particle distribution function is closely associated with fluid density and momentum. Thus, the variation of density across the interface will result in a variation of the particle distribution functions. When the density ratio of two fluids is large, the large variation of the particle distribution functions will cause severe numerical instability and jeopardise the simulation. To overcome this numerical problem, He $et\ al.$[39] creatively introduced an incompressible transformation to change the particle distribution function for density and momentum to that for pressure and momentum. As pressure is continuous across the interface, the high variation of particle distribution function is avoided. Lee[45] adopted this transformation technique and continuously refined it through a series of stable discretization schemes to enhance numerical stability[47,52,53].

Defining a new particle distribution function

$$g_\alpha = \frac{1}{3}f_\alpha c^2 + (p_1 - \frac{1}{3}\rho c^2)\Gamma_\alpha(0), \tag{9}$$

in which $\Gamma_\alpha(\mathbf{u}) = f_\alpha^{eq}/\rho$ and taking the total derivative $D_t = \partial_t + \mathbf{e}_\alpha \cdot \nabla$ of g_α result in

$$\partial g_\alpha/\partial t + \mathbf{e}_\alpha \cdot \nabla g_\alpha = -(g_\alpha - g_\alpha^{eq})/\lambda + (\mathbf{e}_\alpha - \mathbf{u}) \cdot [\frac{1}{3}\nabla\rho c^2(\Gamma_\alpha - \Gamma_\alpha(0)) - C\nabla\mu\Gamma_\alpha] \tag{10}$$

where the new equilibrium g_α^{eq} is

$$g_\alpha^{eq} = \omega_\alpha\big[p_1 + \rho((\mathbf{e} \cdot \mathbf{u}) + 3(\mathbf{e}_\alpha \cdot \mathbf{u})^2/2c^2 - u^2)\big] \tag{11}$$

Discretizing Eq. (10) along characteristics over the time step δt, we obtain the LBE for g_α

$$\bar{g}_\alpha(\mathbf{x}+\mathbf{e}_\alpha\delta t, t+\delta t) = \bar{g}_\alpha(\mathbf{x},t) - \frac{1}{\tau+0.5}(\bar{g}_\alpha - \bar{g}_\alpha^{eq})|_{(\mathbf{x},t)} + (\mathbf{e}_\alpha - \mathbf{u}) \cdot [\frac{1}{3}\delta t\nabla^{MD}\rho c^2(\Gamma_\alpha(\mathbf{u}) - \Gamma_\alpha(0)) - C\delta t\nabla^{MD}\mu\Gamma_\alpha]|_{(\mathbf{x},t)} \tag{12}$$

where ∇^{MD} and ∇^{CD} are referred to mixed difference approximation and central difference approximation respectively[47] and $\tau(=\lambda/\delta t)$ is the non-dimensional relaxation time. In Eq. (12), the modified particle distribution function $\bar{g}_\alpha$ and the equilibrium distribution function $\bar{g}_\alpha^{eq}$ are introduced to facilitate computation

$$\bar{g}_\alpha = g_\alpha + \frac{1}{2\tau}(g_\alpha - g_\alpha^{eq}) - \frac{1}{2}\delta t(\mathbf{e}_\alpha - \mathbf{u}) \cdot \left[\frac{1}{3}\nabla^{CD}\rho c^2 C(\Gamma_\alpha(\mathbf{u}) - \Gamma_\alpha(0)) - C\nabla^{CD}\mu\Gamma_\alpha\right] \tag{13}$$

$$\bar{g}_\alpha^{eq} = g_\alpha^{eq} - \frac{1}{2}\delta t(\mathbf{e}_\alpha - \mathbf{u}) \cdot \left[\frac{1}{3}\nabla^{CD}\rho c^2(\Gamma_\alpha(\mathbf{u}) - \Gamma_\alpha(0)) - C\nabla^{CD}\mu\Gamma_\alpha\right] \tag{14}$$

The momentum and hydrodynamic pressure are the zeroth- and first-order moment of $\bar{g}_\alpha$, computed as.

$$\rho u = \frac{3}{c^2}\sum \mathbf{e}_\alpha\bar{g}_\alpha - \frac{\delta t}{2}C\nabla^{CD}\mu \tag{15}$$

$$p_1 = \sum \bar{g}_\alpha + \frac{\delta t}{6}\mathbf{u} \cdot \nabla^{CD}\rho c^2 \tag{16}$$

For the transformation of the composition C, a second distribution function is introduced in a simple format of

5

$h_\alpha = (C/\rho)f_\alpha$ and $h_\alpha^{eq} = (C/\rho)f_\alpha^{eq}$. Similarly, taking the total derivative D_t of h_α and utilizing Eq. (3) yield

$$\bar{h}_\alpha\left(\mathbf{x}+\mathbf{e}_\alpha\delta t,\, t+\delta t\right)=\bar{h}_\alpha\left(\mathbf{x},\, t\right)-\frac{(\bar{h}_\alpha-\bar{h}_\alpha^{eq})\,|_{(\mathbf{x},\,t)}}{\tau+0.5}+\delta t\,(\mathbf{e}_\alpha-\mathbf{u})[\nabla^{MD}C-\frac{3C}{\rho c^2}\left(\nabla^{MD}p+C\nabla^{MD}\mu\right)]\Gamma_\alpha|_{(\mathbf{x},\,t)}+\delta tM\nabla^2\mu\,\Gamma_\alpha|_{(\mathbf{x},\,t)}$$

$$(17)$$

where the modified particle distribution function $\bar{h}_\alpha$ and $\bar{h}_\alpha^{eq}$ are defined as [47]

$$\bar{h}_\alpha = h_\alpha + \frac{1}{2\tau}(h_\alpha - h_\alpha^{eq}) - \frac{\delta t}{2}(\mathbf{e}_\alpha - \mathbf{u}) \cdot [\nabla^{CD}C - \frac{3C}{\rho c^2}(\nabla^{CD}p + C\nabla^{CD}\mu)]\Gamma_\alpha \tag{18}$$

$$\bar{h}_\alpha^{eq} = h_\alpha^{eq} - \frac{\delta t}{2}(\mathbf{e}_\alpha - \mathbf{u}) \cdot [\nabla^{CD}C - \frac{3C}{\rho c^2}(\nabla^{CD}p + C\nabla^{CD}\mu)]\Gamma_\alpha \tag{19}$$

The composition C is the zeroth-order moment of $\bar{h}_\alpha$ computed as.

$$C = \sum_\alpha \bar{h}_\alpha + 0.5\delta tM\nabla^2\mu \tag{20}$$

As discussed in reference [53], the interfacial mobility M in Eq. 20 plays a role to suppress the nonphysical parasitic currents caused by the numerical discretization. M should be chosen carefully large enough so that the diffusion maintain the interface near its equilibrium state but small enough to avoid damping the flow near the interface. In the present study, we set $M(= 6.67)$ as a constant as suggested. The density ρ and the dimensionless relaxation frequency $(1/\tau)$ are taken as linear functions of the composition by

$$\rho(C) = C\rho_1 + (1 - C)\rho_2, \quad 1/\tau(C) = C/\tau_1 + (1 - C)/\tau_2 \tag{21}$$

Computational Set-up

In this work, we simulate coalescence of two unequal microbubbles in a square domain with the side length of $100(\mu m)$. To distinguish the parent bubbles, we denote the large bubble as father (F) with radius r_F and the small one as mother (M) with r_M. The size inequality of the parent bubbles, γ, is defined by the ratio of the radii, r_F/r_M. For the purpose to explore the effects of size inequality on bubble coalescence, we fix the size of the father bubble as $r_F = 20(\mu m)$ and vary r_M from $3.75(\mu m)$ to $20(\mu m)$, resulting in a range of γ from 5.33 to 1. Correspondingly, Ohnesorge number $Oh(= \eta_w/\sqrt{\rho_w\sigma r_M})$, a dimensionless parameter defined as the ratio of internal viscosity vs. surface tension, varies from 6.1×10^{-2} to 2.6×10^2. Table 1 lists r_M, γ, and Oh values for twelve cases, among which $\gamma = 1$ is a limited case corresponding to equal-size coalescence. Water is filled in the domain. With the origin $(0,0)$ of a Cartesian coordinate system at the south-west corner of domain, F is placed at $x = 30(\mu m)$ and $y = 50(\mu m)$ and M is attached to F at the same height. Thus, the mother bubble with radius r_M is located at $x = 50 + r_M(\mu m)$ and $y = 50(\mu m)$. The density and viscosity of water and air are $\rho_w = 1 \times 10^3(kg/m^3)$, $\rho_a = 1.2(kg/m^3)$ and $\eta_w = 1 \times 10^{-3}kg/(m \cdot s)$, $\eta_a = 1.98 \times 10^{-5}kg/(m \cdot s)$ respectively, resulting in the density ratio and viscosity ratio of water vs. air, 833 and 50.5 respectively. The surface tension between water and air is assumed to be $7.2 \times 10^{-2}N/m$. Such a physical setup is used in the entire study unless otherwise indicated.

We choose D2Q9 lattice model [32] with $\alpha = 0, 1, 2, \cdots, 8$ for the simulation. The discrete velocities of $\mathbf{e}_\alpha$ are given by 0 for $\alpha = 0$, $(\cos[(\alpha - 1)\pi/2], \sin[(\alpha - 1)\pi/2])$ for $\alpha = 1 - 4$, and $\sqrt{2}(\cos[(2\alpha - 9)\pi/2], \sin[(2\alpha - 9)\pi/2])$ for

$\alpha = 5-8$ with the directional weight factor ω_α as 4/9 for $\alpha = 0$, 1/9 for $\alpha = 1-4$, and 1/36 for $\alpha = 5-8$. In order to focus on the bubble coalescence with no boundary effects, we use periodic boundary in each direction. While the formation of LBEs in the above section seems complicated, the implementation of them is straightforward. The parameters in lattice unit are selected as $\rho_w = 1.0$, $\rho_a = 0.0012$, $\sigma = 10^{-3}$, $D = 4$, $\beta = 12\sigma/D = 0.003$, $\kappa = 3/2\sigma D$, $\tau_w = 0.022361$, and $\tau_a = 0.3682$. The relation between simulation time (in time step) and physical time (in second), denoted by superscripts "l" and "p" respectively, is formulated through the dimensionless parameter Oh for water as $t^p/t^l = (l^p)^{\frac{3}{2}}/(3(l^l)^{\frac{3}{2}})\sqrt{\rho_w^p \sigma^l/\rho_w^l \sigma^p}$ noticing that the $l^l = l^p/N_x$ and $\nu^p/\nu^l = t^l/(l^l)^2$. The initial conditions are set as $p_1 = 0$, $\mathbf{u} = 0$, C, ρ, τ, μ, $\bar{h}^{eq}$, and $\bar{g}^{eq}$ are calculated by Eqs. (5), (21), (21), (4), (19), and (14) respectively. Time iteration includes [1] collision: the right-hand sides of Eqs. (17) and (12) respectively; [2] streaming: the left-hand sides of Eqs. (17) and (12) respectively; and (3) macroscopic variable update: C, ρ, τ, $\rho\mathbf{u}$, p_1, $\bar{h}^{eq}$, and $\bar{g}^{eq}$ by Eqs. (20), (21), (21), (15), (16), (19), and (14) correspondingly. Before we produce numerical results, we conduct basic checks and validations.

Convergence check Maintaining the physical size of the bubble and flow domain, we use five spatial resolutions of 100^2, 200^2, 300^2, 400^2, and 800^2 to simulate the father bubble starting from the initial conditions described above, respectively. When the bubble reaches a steady state, the pressure difference across the air-water interface is calculated by $\triangle p = p_a - p_w$ in which p_a and p_w are the pressure value where $dp/dx \simeq 0.0$ adjacent the diffusive interface in air and water sides respectively. It is found that the relative errors of $\triangle p$ over the analytical prediction from Laplace theory, $\triangle p = \sigma/R = 3.6kPa$, corresponding to the above resolution sequence are 12.1%, 1.95%, 1.1%, 0.63%, and 0.34%.

Laplace-law check We use 400^2 as the spatial resolution to produce the relationship between $\triangle p$ and r_F and compare with Laplace law as a validation. Six microbubbles with the radius from $20 - 40(\mu m)$ are simulated. The dependence of $\triangle p$ to $1/r_F$ is shown in Fig. 1. It is seen that the simulation results (symbols) agree well with the analytical prediction (line) for this large density and viscosity ratio case, demonstrating the validity of the LBM modeling and simulation.

Mass conservation check As shown in Table 2, the relative mass changes before and after 2000 time steps are compared for four inequality cases of $\gamma = 4, 2, 1.33$, and 1. The mass change per time step is about 5.0×10^{-8}, which is acceptable for mass conservation.

Numerical Results

We now present numerical results on bubble coalescence.

Spatial and temporal scaling of coalescence

The time evolution of bubble coalescence for the case of $\gamma = 1.6$, $Oh = 3.3 \times 10^{-2}$ in Table 1 is shown in Fig. 2. The air-water interface is depicted by the contour line of $\rho = 0.5$. The coalescence takes $142\mu s$ evolving from two attached parent bubbles (a) to a coalesced perfect bubble (f) going through asymmetrical dumbbell(b), egg(c), oval(d), and elliptical circle (e) shape. Fig. 3 shows bubble coalescence processes in a stacked format

with four different γs: (a) 4.0, (b) 2.0, (c) 1.33, and (d)1.0. The corresponding Ohs are 5.2×10^{-2}, 3.7×10^{-2}, 3×10^{-2}, and 2.6×10^{-2}. In each case, the bubble coalescence process from initially two attached bubbles (black dash line) to finally one perfect coalesced bubble (black solid). Three intermediate stages are denoted by red, green, and pink colors successively. The time is indicated with the same color correspondingly. While the time evolution of the air-water interface of each case is seen similar to that shown in Fig. 2, there are two effects of size inequality on the coalescence. First, the perfected coalesced bubble (black solid line) merged from two unequal parent bubbles (black dashed lines) tends to locate closer to the father bubble. This phenomenon is so called "coalescence preference", recently observed in experiments[29,30]. The preference can be quantified by the relative distance ratio of $\chi = d_{FC}/d_{MC}$, in which d_{FC} and d_{MC} are the distances of the centers of father bubble (O_F) and mother bubble (O_M) to coalesced bubble respectively, as schematized in Fig. 4. As obtained in the experiments, the preferential distance ratio χ exhibits power-law relationship to the size inequality as $\chi \sim \gamma^{-p}$. Such a spatial power-law scaling is captured in the current numerical study. In Fig. 5, red and green symbols are experimental results from Fig. 4 in[30] and Fig. 2 in[29] respectively, and black symbols are from the current simulation. Power-law fitting of the three data sets result in $p = 3.992$ (red[30]), 2.152(green[29]), and 2.079 (black). The discrepancies among the three scaling are due to the different fluids and different set-up in the experiments and current simulation. As seen in Figs. 2 and 3, larger γ corresponds to faster coalescence. The equal size case shown in Fig. 3(d) takes the longest time, i.e. $T = 223\mu s$, to complete its coalescence while the largest inequality case, $\gamma = 4$ (Fig. 3(a)), takes to shortest time, $T = 77\mu s$, to complete the coalescence. It is found that the coalescence time T from two parent bubbles to a coalesced perfect bubble also exhibits a power-law relationship to the size inequality as $T \sim \gamma^{-q}$, as shown in Fig. 6. The solid line is the trendline fitted by power-law for the symbols obtained from the simulation with $R^2 = 0.9785$. Such a power-law relationship is believed to be the first time observation.

Dynamics of microbubble coalescence

To understand the underlying physics behind the power-law spatial and temporal scaling of bubble coalescence, we look into the time evolution of coalescence for the case of $\gamma = 1.6$ and $Oh = 3.3 \times 10^{-2}$. The coalescence in terms of the air-water interface evolution has been shown and interpreted in Fig. 2. Fig. 7 and 8 show the pressure and velocity fields at (a) $t = 5\mu s$, (b) $42\mu s$, and (c) $80\mu s$. Shortly after the two parent bubbles are attached, i.e. (a) $t = 5\mu s$, the interface exhibits an asymmetrical dumbbell shape with a neck at the location where the two parent bubbles were originally attached. Large pressure at both edges of the father and mother bubbles and the small pressure at the neck (Fig. 7(a)) are seen and the pressure difference between the edge and neck is large. Air swarms from two edges toward the neck in the horizontal direction, stronger from the mother bubble side than the father. These two streams meet and interact inside the neck, spouting the flow along both sides in the vertical direction (Fig. 8(a)). Two pairs of attached and opposite vortices are formed at the top and bottom interface respectively. Such a flow pattern stretches the neck in an opposite direction vertically, more on the mother bubble size than the father. At an intermediate time, $t = 42\mu s$, the asymmetrical dumbbell shape has been stretched as an egg shape

with a tip and a base at left and right respectively. Higher pressure is developed at both the tip and base end but the pressure difference between the two ends drops (Fig. 7(b)). As seen in Fig. 8(b), air continues to flow face to face horizontally, stronger from the tip side than the base side.

The location where horizontal flow streams meet and vertical streams leave are moved to the left. The opposite vortices at the top and bottom move apart to the tip and base area. Due to the unbalanced pressure and flow in horizontal direction, the interface is still stretched along the vertical direction stronger in the tip than the base side, reducing the curvature difference of the tip and base of the egg. At a later time, $t = 80\mu s$, additional larger pressure is developed at the farmost horizontal interface with vanishing difference (Fig. 7(c)). The interface appears as an elliptical circle with similar curvature horizontally (Fig. 8(c)). Two vortex pairs are formed similarly in both horizontal and vertical directions. Horizontal streams meet at the center of the bubble and leave along both sides of vertical direction with similar velocity. The interface is further stretched along both sides of vertical direction toward minimum surface energy. Figs. 9, 10, and 11 provide the quantitative information regarding to the flow of dynamics in the coalescence.

Summary and Future Work

We have numerically studied the microbubble coalescence using the lattice Boltzmann simulation. The "coalescence preference" that the coalesced bubble is located closer to the larger parent bubble is well captured. The preferential location of the coalesced bubble is a function of size inequality, the radius ratio of the father (large) to mother (small) bubble $\gamma = r_F/r_M$. Systematical simulation of 12 cases varying the size inequality γ from 5.33 to 1 results in a power-law relation between the preferential relative distance χ and size inequality γ as $\chi \sim \gamma^{-2.079}$, which is consistent to the recent experimental observations. Meanwhile, we found that the coalescence time is also correlated to the size inequality through a power-law relation, $T \sim \gamma^{-0.7}$, implying that unequal-size bubbles always coalesce faster than equal-size bubbles and that the larger the size inequality is, the faster they coalesce. Such a temporal scaling of coalescence on inequality size ratio is believed to be a first time observation. Due to the fast occurrence of microbbule coalescence in the order of micro-second, such a temporal scaling is hard to be captured through laboratory experimentation. In order to better understand the underlying physics behind the spatial and temporal scaling, we show the detailed dynamics at early, intermediate, and relatively late time periods in a representative coalescence with $\gamma = 1.6, Oh = 3.3 \times 10^{-2}$. Due to the unbalanced pressure at the horizontal farmost edges of father and mother bubbles, there is larger pressure at the mother bubble side than the father; two unbalanced horizontal flow streams; stronger streams at the mother bubble size than the father, swarm face to face to the neck area and spout the flow along both sides of vertical direction. As a result, the emerging bubble is stretched at the neck or the minor curvature area. Such a flow pattern maintains until equal curvature on both horizontal sides are reached. Then, the balanced horizontal streams move toward the center of the merging bubble and squeeze the flow up and down to elongate the vertical axis until a perfect child bubble forms. In a typical coalescence from two unequally sized parent bubbles to a coalesced bubble, the topological geometry of the two-fluid

9

interface undergoes a sequence of asymmetrical dumbbell, egg, oval, and elliptical circle.

The results of this study has inspired more sophisticate investigation regarding the spatial and temporal scaling of microbubble coalescence in the following aspects.

1. Three-dimensional simulation to confirm the scaling. Richer dynamics is expected to better understand the physics underling the coalescence preference.

2. The effects of density ratio, viscosity ratio, bubble size, Oh value, etc. on the spatial and temporal scaling.

3. Microbubble coalescence in a channel with touching solid boundaries.

It is believed that the coalescence spatial and temporal scaling are universally important in understanding the stability and the statistics of coalescing bubbles and would impact on a variety of engineering, industrial, medical, and pharmacological applications.   fnameLiterature Cited

References

1. Ferrara K, Pollard R, Borden M. Ultrasound microbubble contrast agents: fundamentals and application to gene and drug delivery. *Annu. Rev. Biomed. Eng..* 2007;9:415–447.

2. Sirsi S, Borden M. Microbubble Compositions, Properties and Biomedical Applications. *Bubble Sci Eng Technol..* 2009;1:3 – 17.

3. Qin S, Caskey CF, Ferrara KW. Numerical simulation of hemodynamics in intracranial saccular aneurysm treated with a novel stent. *Phys Med Biol..* 2009;54:R27 — 57.

4. Kang ST, Yeh CK. Lattice Boltzman method for reacting flows in porous mediaUltrasound microbubble contrast agents for diagnostic and therapeutic applications: current status and future design. *Chang Gung Med J..* 2012;35:125–39.

5. Lindner J, Jayaweera AR, Sklenar J, Kaul S. Microvascular rheology of Definity microbubbles after intra-arterial and intravenous administration. *J Am Soc Echocardiogr..* 2002;15:396 — 403.

6. Matsuki N, Ichiba S, Ishikawa T, et al. Blood oxygenation using microbubble suspensions. *European Biophysics Journal.* 2012;41:571–578.

7. Unger EC, Porter T, Culp W, Labell R, Matsunaga T, Zutshi R. Therapeutic applications of lipid-coated microbubbles. *Advanced drug delivery reviews.* 2004;56:1291–1314.

8. Ibsen S, Schutt EC, Esener S. Microbubble-mediated ultrasound therapy: a review of its potential in cancer treatment. *Drug Des Devel Ther..* 2013;7:375 – 388.

9. Terasaka K, Hirabayashi A, Nishino T, Fujioka S, Kobayashi D. Development of microbubble aerator for waste water treatment using aerobic activated sludge. *Chemical engineering science.* 2011;66:3172–3179.

10. Ashutosh Agarwal A, Ng WJ, Liu Y. Principle and applications of microbubble and nanobubble technology for water treatment. *Chemosphere.* 2011;84:1175 - 1180.

11. Khuntia S, Majumder S, Ghosh P. Microbubble-aided water and wastewater purification: a review. *Reviews in Chemical Engineering.* 2012;28:191–221.

12. Kaushik G, Chel A. Microbubble technology: emerging field for water treatment. *Bubble Science, Engineering & Technology.* 2014;5:33-38.

13. Tesar V, Peszynski K. Water oxygenation by fluidic microbubble generator. *EPJ Web of Conferences.* 2014;67:02116.

14. Dittrich PS, Manz A. Lab-on-a-chip: microfluidics in drug discovery. *Nature Reviews Drug Discovery.* 2006;5:210–218.

15. Chung SK, Rhee K, Cho SK. Bubble actuation by electrowetting-on-dielectric (EWOD) and its applications: A review. *International Journal of Precision Engineering and Manufacturing.* 2010;11:991 – 1006.

16. Zimmerman WB, Hewakandamby BN, Tesař V, Bandulasena HCH, Omotowa OA. On the design and simulation of an airlift loop bioreactor with microbubble generation by fluidic oscillation. *Food and Bioproducts Processing.* 2009;87:215–227.

17. AL-Mashhadani MKH, Wilkinson JS, Zimmerman BW. Airlift bioreactor for biological applications with microbubble mediated transport processes. *Chemical Engineering Science.* 2015;137:243 - 253.

18. Chambers Richard D, Holling Darren, Spink Robert CH, Sandford Graham. Elemental fluorine Part 13. Gas–liquid thin film microreactors for selective direct fluorination. *Lab on a Chip.* 2001;1:132–137.

19. Kobayashi J, Mori Y, Okamoto K, et al. A microfluidic device for conducting gas-liquid-solid hydrogenation reactions. *Science.* 2004;304:1305–1308.

20. Zhu L, Kroodsma N, Yeom J, Haan JL, Shannon MA, Meng DD. An on-demand microfluidic hydrogen generator with self-regulated gas generation and self-circulated reactant exchange with a rechargeable reservoir. *Microfluidics and nanofluidics.* 2011;11:569–578.

21. Burns MA, Johnson BN, Brahmasandra SN, et al. An integrated nanoliter DNA analysis device. *Science.* 1998;282:484–487.

22. Lessard RR, Zieminski SA. Bubble coalescence and gas transfer in aqueous electrolytic solutions. *Ind. Eng. Chem. Fundam..* 1971;10:260–269.

23. Stover RL, Tobias CW, Denn MM. Bubble coalescence dynamics. *AIChE J.* 1997;43:2385—2392.

24. Liao YX, Lucas D. A literature review on mechanisms and models for the coalescence process of fluid particles. *Chem. Eng. Sci.*. 2010;65:2851— 2864.

25. Javier RRJ, Sevilla A, Martinez-Bazan C, Gordillo JM. Generation of Microbubbles with Applications to Industry and Medicine. *Annu. Rev. Fluid Mech.*. 2015;47:405–429.

26. Vakarelski IU, Manica R, Tang X, et al. Dynamic interactions between microbubbles in water. *PNAS*. 2010;107:11177—11182.

27. Yang L, Wang K, Tan J, Lu Y, Luo G. Experimental study of microbubble coalescence in a T-junction microfluidic device. *Microfluid Nanofluid*. 2012;12:715–722.

28. Paulsen JD, Carmigniani R, Kannan A, Burton JC, Nagel SR. Coalescence of bubbles and drops in an outer fluid. *Nature Communications*. 2014;5:3182–3199.

29. Kim Y, Lim SJ, Gim B, Weon BM. Coalescence preference in densely packed microbubbles. *Scientific Reports*. 2015;5:7739.

30. Weon BM, Je JH. Coalescence preference depends on size inequality. *Physical review letters*. 2012;108:224501.

31. Chen HD, Chen SY, Matthaeus WH. Recovery of the Navier-Stokes Equations Using Lattice-gas Boltzmann Method. *Physical Review A*. 1992;45:R5339–R5342.

32. Qian YH, Dhumieres D, Lallemand P. Lattice Boltzmann Model for Navier-Stokes Equation. *Europhysics Letters*. 1992;17:479–484.

33. Chen S, Doolen GD. Lattice Boltzmann method for fluid flows. *Annual Review of Fluid Mechanics*. 1998;30:329–364.

34. Aidun CK, Clausen JR. Lattice-Boltzmann Method for Complex Flows. *Annual Review of Fluid Mechanics*. 2010:439–472.

35. Andrew K. Gunstensen KA, Daniel H Rothman HD, Zaleski S, Zanetti G. Lattice Boltzmann model of immiscible fluids. *Phys. Rev. A*. 1991;43:4320–27.

36. Shan XW, Chen HD. Lattice Boltzmann Model for Simulating Flows with Multiphases and Components. *Physical Review E*. 1993;47:1815–1819.

37. Shan XW, Chen HD. Simulation of nonideal gases and liquid-gas phase transitions by the lattice Boltzmann equation. *Physical Review E*. 1994;49:2941–2948.

38. He XY, Shan X, Doolen GD. Discrete Boltzmann equation model for nonideal gases. *Physical Review E*. 1998;57:R13.

39. He X, Chen S, Zhang R. A Lattice Boltzamnn Scheme for Incompressible Multiphase Flow and its Application in Simulation of Rayleigh-Taylor Instability. *J. Comp. Phys.*. 1999;152.

40. Swift MR, Osborn WR, Yeomans JM. Lattice Boltzmann simulation of nonideal fluids. *Phys. Rev. Let.*. 1995;75:830-833.

41. Swift MR, Orlandini E, Osborn WR, Yeomans JM. Lattice Boltzmann simulations of liquid-gas and binary fluid systems. *Physical Review E*. 1996;54:5041-5052.

42. Mazloomi M A, Chikatamarla SS, Karlin IV. Entropic Lattice Boltzmann Method for Multiphase Flows. *Phys. Rev. Lett.*. 2015;114:174502.

43. Chen L, Qinjun Kang Q, Mua Y, He Y-L, Tao W-Q. A critical review of the pseudopotential multiphase lattice Boltzmann model: Methods and applications. *International Journal of Heat and Mass Transfer*. 2014;76:210 – 236.

44. Connington K, Lee T. A review of spurious currents in the lattice Boltzmann method for multiphase flows. *Journal of Mechanical Science and Technology*. 2012;26:3857–3863.

45. Lee T, Lin C-L. A stable discretization of the lattice Boltzmann equation for simulation of incompressible two-phase flows at high density ratio. *J. Comp. Phys.*. 2005;206:16 — 47.

46. Ding H, Spelt PDM, Shu C. Diffuse interface model for incompressible two-phase flows with large density ratios. *J. Comp. Phys.*. 2007;226:2078 – 2095.

47. Lee T, Liu L. Lattice Boltzmann simulations of micron-scale drop impact on dry surfaces. *J Comp Phys*. 2010;229:8045–8063.

48. Shan JY, Shu C, Huang HB, Chew YT. Free-energy-based lattice Boltzmann model for the simulation of multiphase flows with density contrast. *Physical Review E*. 2014;89:033309.

49. Cahn JW, Hilliard JE. Free Energy of a Nonuniform System. I. Interfacial Free Energy. *J. Chem. Phys.*. 1958;28:258 — 266.

50. Anderson DM, McFadden GB, Wheeler AA. Diffus-Interface Method in Fluid Mechanics. *Annu. Rev. Fluid Mech.*. 1998;30:139 — 165.

51. Jacqmin D. Calculation of Two-Phase NavierStokes Flows Using Phase-Field Modeling. *J. Comp. Phys.*. 1999;155:96 – 127.

52. Lee T, Fischer PF. Eliminating parasitic currents in the lattice Boltzmann equation method for nonideal gases. *Physical Review E*. 2006;74:046709.

53. Lee T. Effects of incompressibility on the elimination of parasitic currents in the lattice Boltzmann equation method for binary fluids. *Computers and Mathematics with Applications.* 2009;58:987 — 994.

54. Rowlinson JS, Widom B. *Molecular Theory of Capillarity.* Oxford Univ. Press, Oxford, UK 1989.

55. Capuani F, Pagonabarraga I, Frenkel D. Discrete solution of the electrokinetic equations. *J Chem Phys.* 2004;121:973 — 986.

56. Jamet D, Lebaigue O, Coutris N, Delhaye JM. The second gradient method for the direct numerical simulation of liquid–vapor flows with phase change. *Journal of Computational Physics.* 2001;169:624–651.

57. Day MS, Bell JB. Numerical Simulation of Laminar Reacting Flows with Complex Chemistry. *Combust. Theory Model..* 2000;4:535 — 556.

58. Harris M, Coombe G, Scheuermann T, Lastra A. Physically-Based Visual Simulation on Graphics Hardware. *SIGGRAPH/EUROGRAPHICS Workshop on Graphics Hardware.* 2002:109–118.

59. He X, Luo L. Theory of lattice Boltzmann method: From the Boltzmann equation to the lattice Boltzmann equation. *Physical Review E.* 1997;56:6811–6817.

List of Figures

List of Tables

Case	1	2	3	4	5	6	7	8	9	10	11	12
r_M	3.75	5.0	6.25	7.50	8.75	10.0	11.25	12.50	13.75	15.0	17.50	20.0
γ	5.33	4.0	3.20	2.67	2.29	2.0	1.78	1.60	1.45	1.33	1.14	1.0
$Oh \times 10^{-2}$	6.1	5.2	4.7	4.3	4.0	3.7	3.5	3.3	3.2	3.0	2.8	2.6

Table 1: Studied cases of microbubble coalescence noticing $\gamma = 1$ corresponds a limit case of which the parent bubbles are equal.

Ratio γ	Mass change per time step
4	5.01^{-8}
2	5.02×10^{-8}
1.33	5.03×10^{-8}
1	5.5×10^{-8}

Table 2: Mass conservation check
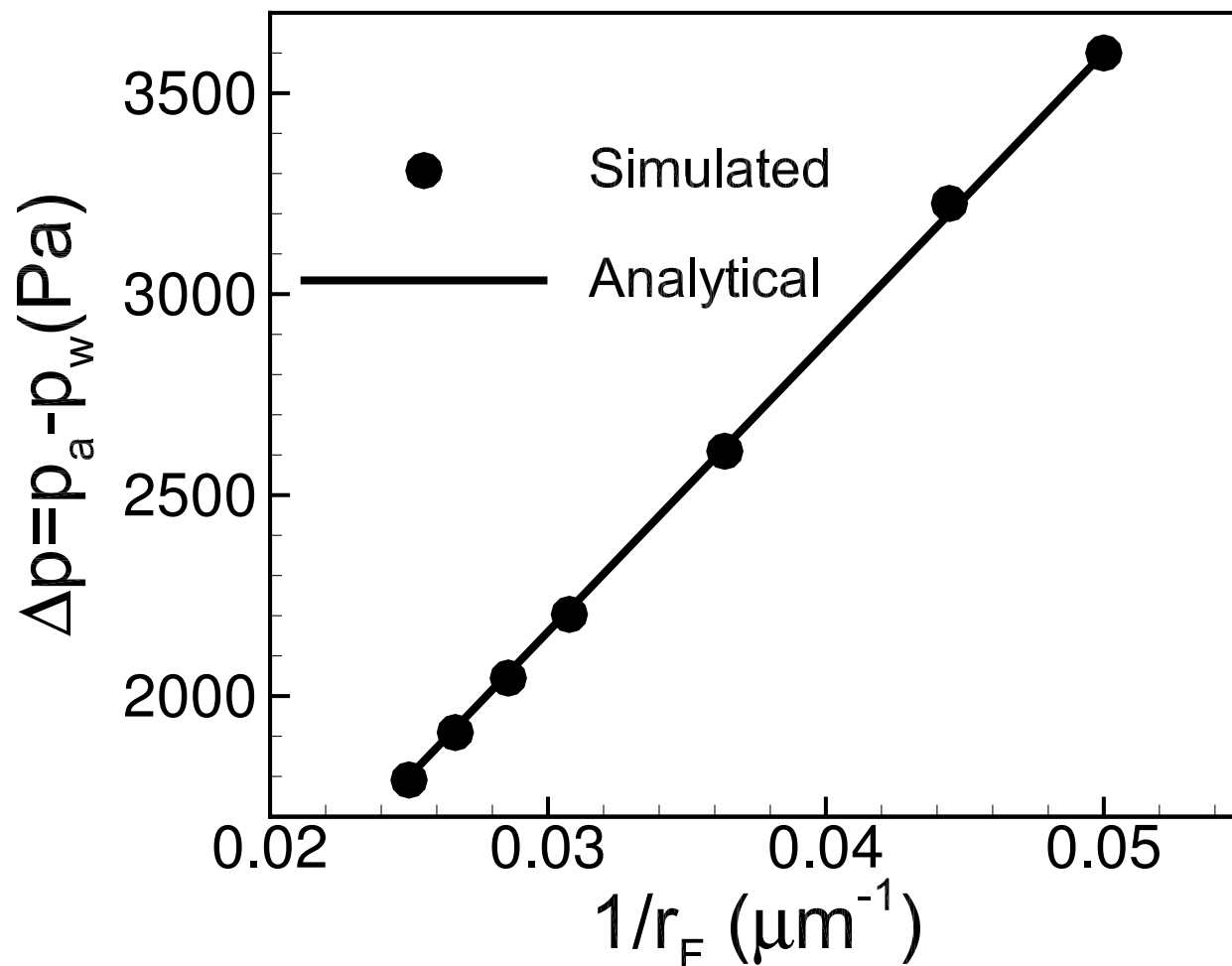
Figure 1: Pressure difference across the diffusive interface $\triangle p$ vs. inverse of radius $(1/r_F)$ via simulation (symbols) and Laplace theory (solid line).
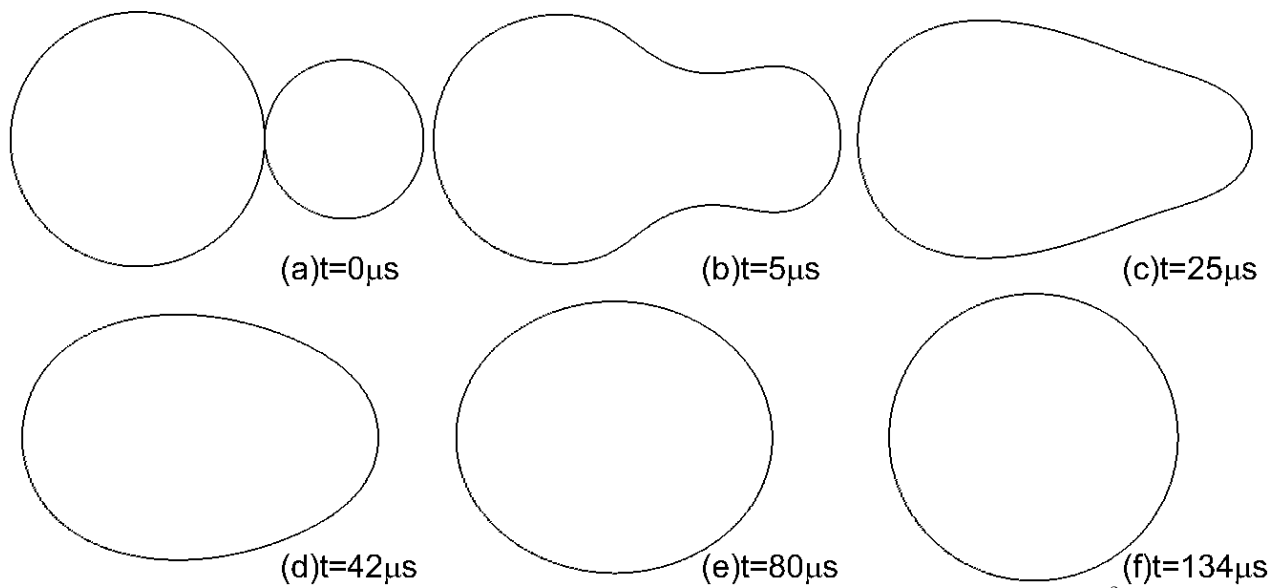
Figure 2: Bubble coalescence depicted by the contour line of $\rho = 0.5$ for the case of $\gamma = 1.6$, $Oh = 3.3 \times 10^{-2}$. The coalescence takes $142\mu s$ changing from initially two attached parent bubbles (a) to a coalesced bubble (f) going through asymmetrical dumbbell(b), egg(c), oval(d), and elliptical circle (e) shape.
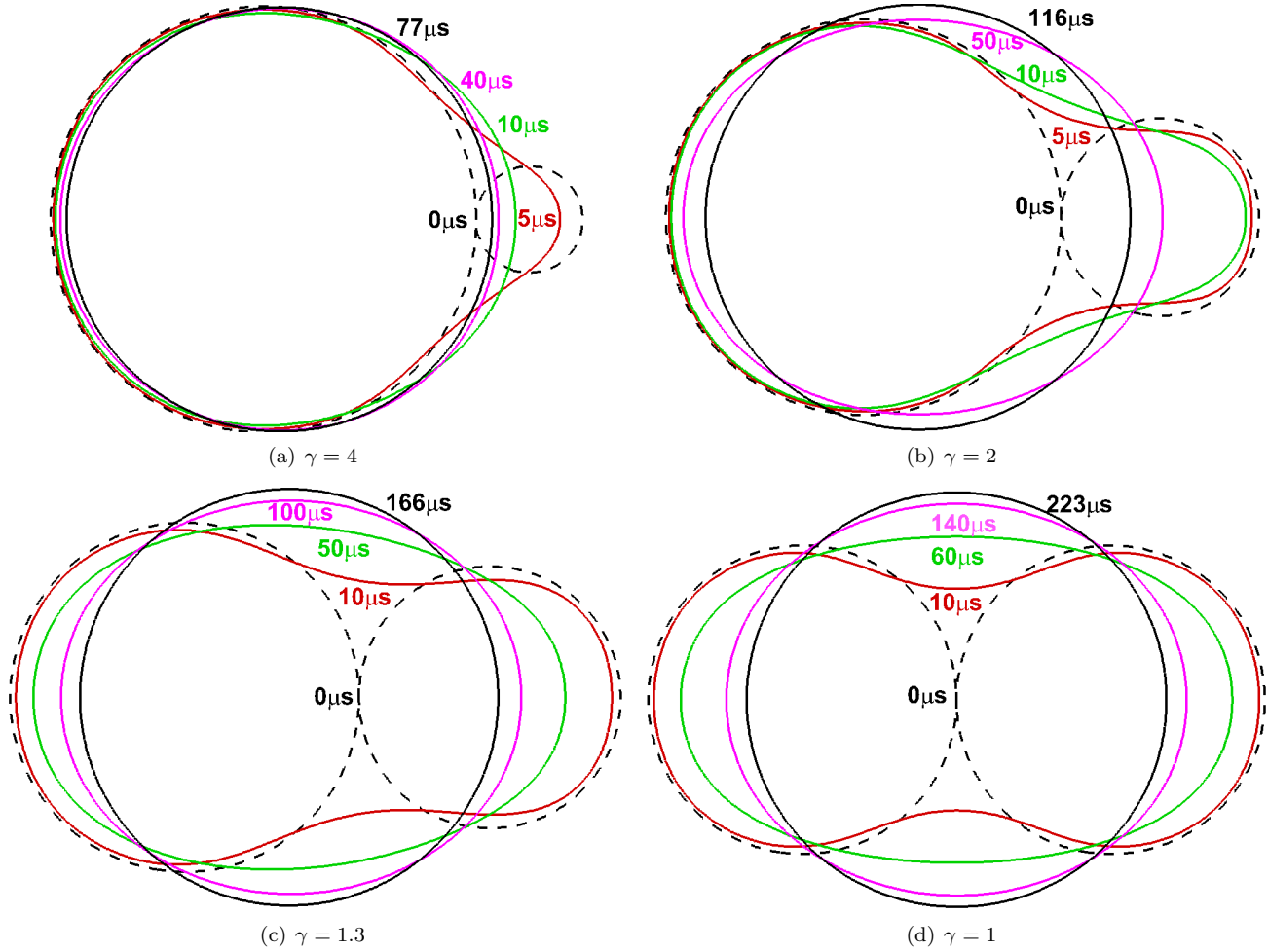
Figure 3: (Color online) Coalescence from two attached parent bubbles (black dashed lines) to one perfectly coalesced bubble (black solid line) with four different size ratios of parent bubbles: $\gamma = (a)4.0$, (b) 2.0, (c)1.33, and (d)1.0 through stacked contour lines of $\rho = 0.5$ at representative time instants. The initial (before coalescence) and final (fully merged) water-air interfaces are recognized by the black dashed and solid lines. Three intermediate shapes evolving successively are denoted in red, green, and pink respectively. The coalescence time, seen as (a)$77\mu s$, (b)$116\mu s$, (c)$166\mu s$, and (d)$223\mu s$, increases when γ decreases.
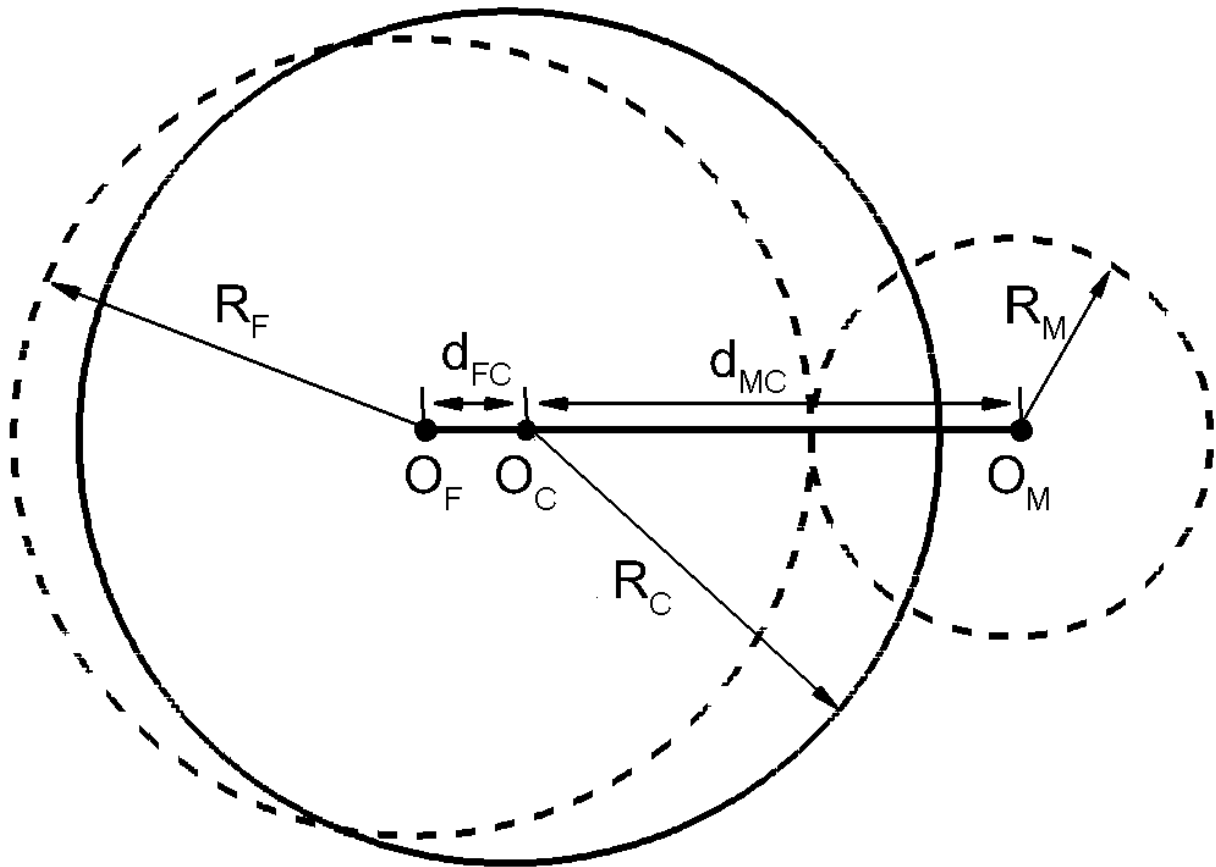
Figure 4: Schematics of coalescence geometry between before (dashed line) and after (solid line) coalescence.
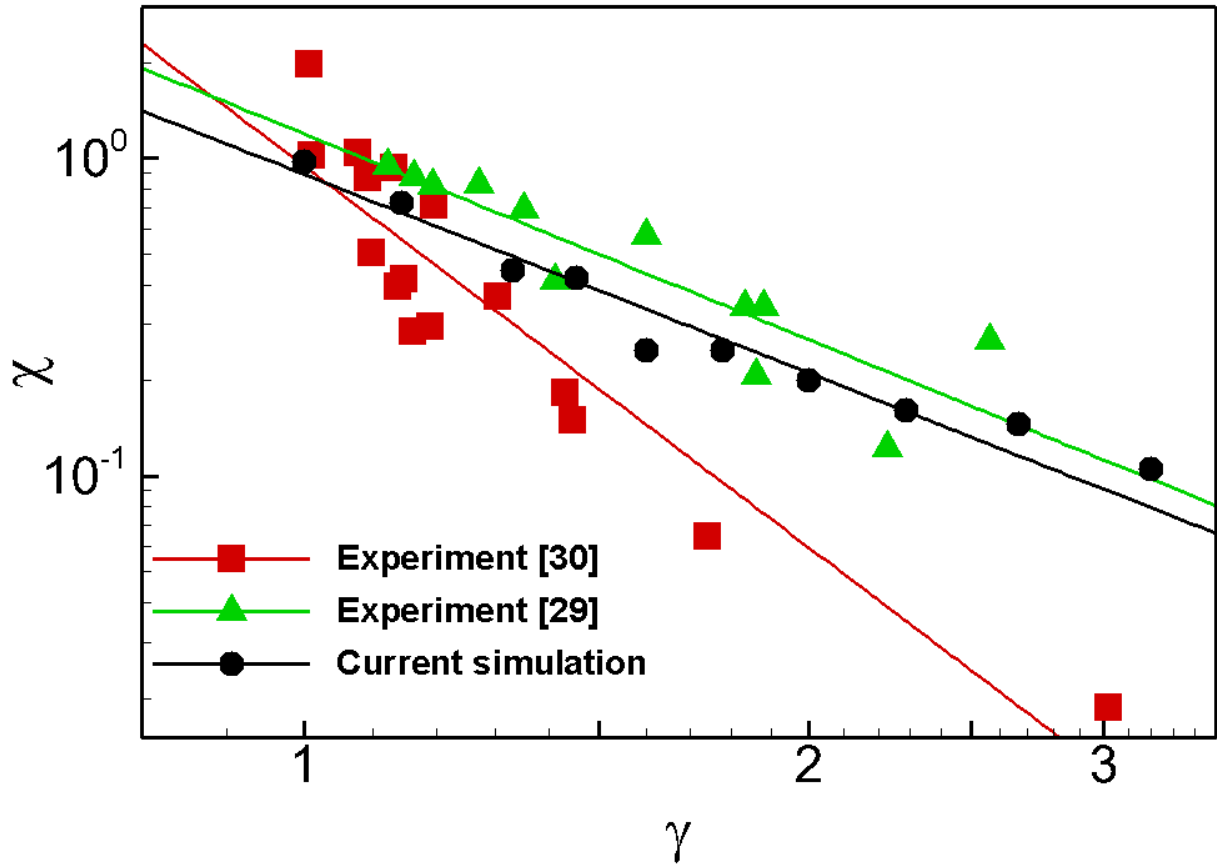
Figure 5: (Color online)Power-law spatial scaling of $\chi(=d_L/d_S) \sim \gamma^{-p}$ in log-log scale. Symbols are experimental and simulation results and lines are power-law fitting corresponding the same color. $p = 3.992$ (red), 2.152 (green), and 2.079 (black, current simulation).
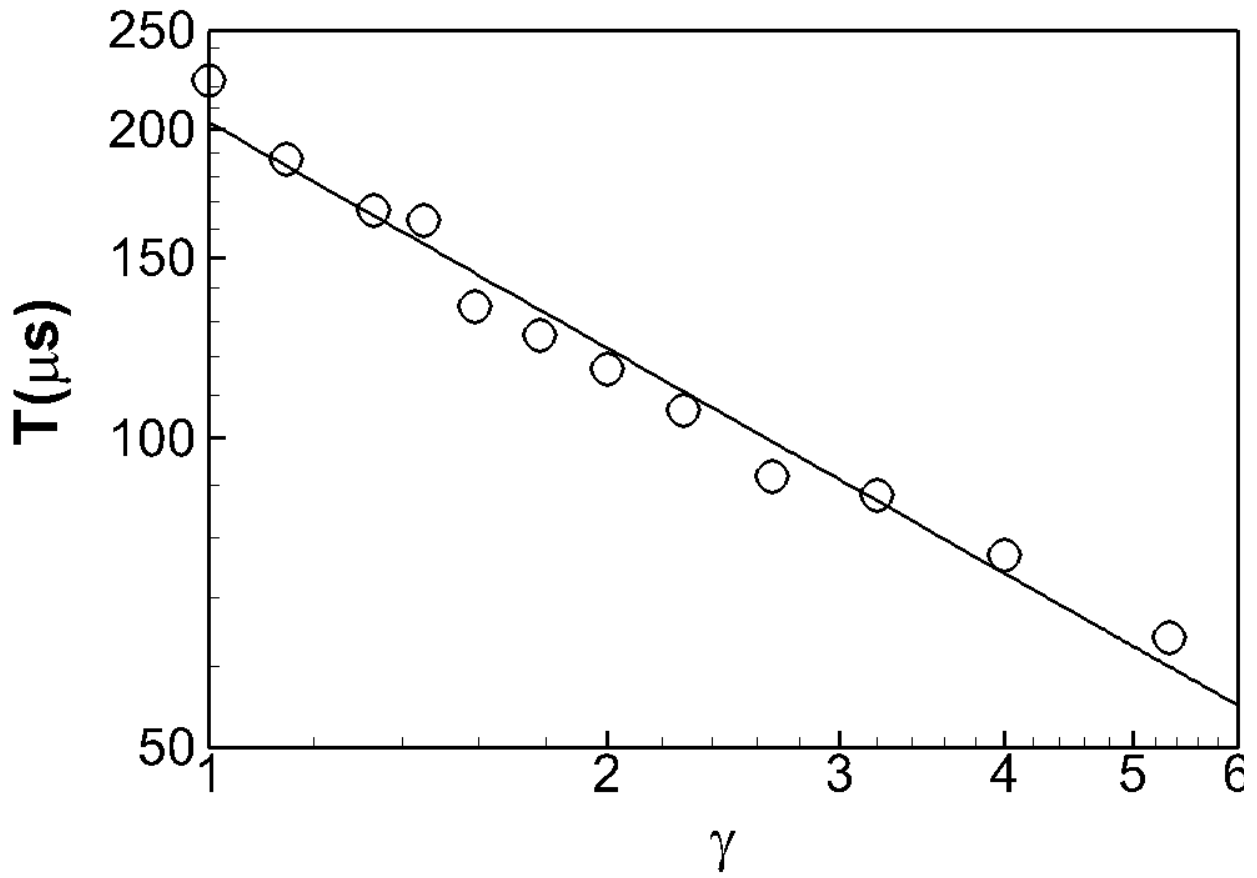
Figure 6: Power-law temporal scaling of $T \sim \gamma^{-q}$ in log-log scale. Symbols are simulation results and line is from a power-law fitting with $q = 0.7$ and $R^2 = 0.9785$.
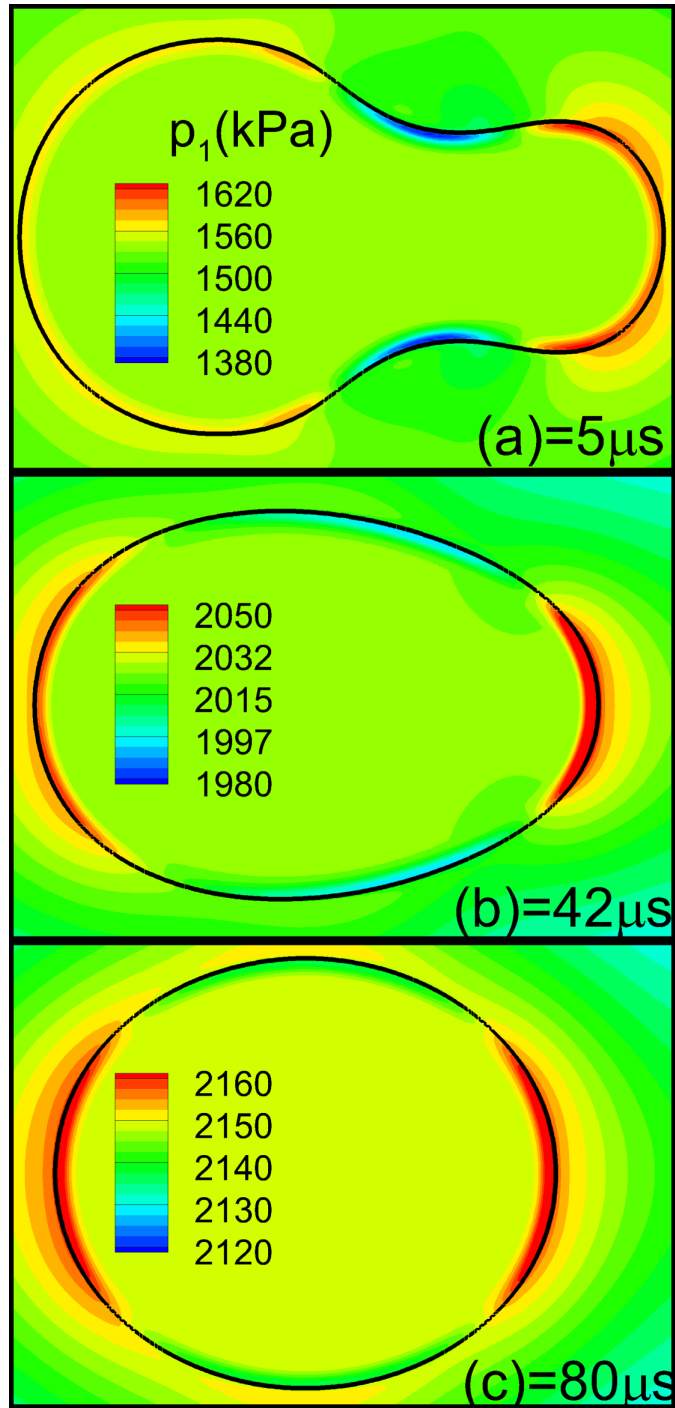
Figure 7: (Color online) Dynamics pressure fields at three representative time instants in the bubble coalescence for the case of $\gamma = 1.6$, $Oh = 3.3 \times 10^{-2}$:(a)$t = 5\mu s$, (b)$t = 42\mu s$, and (c)$t = 80\mu s$.
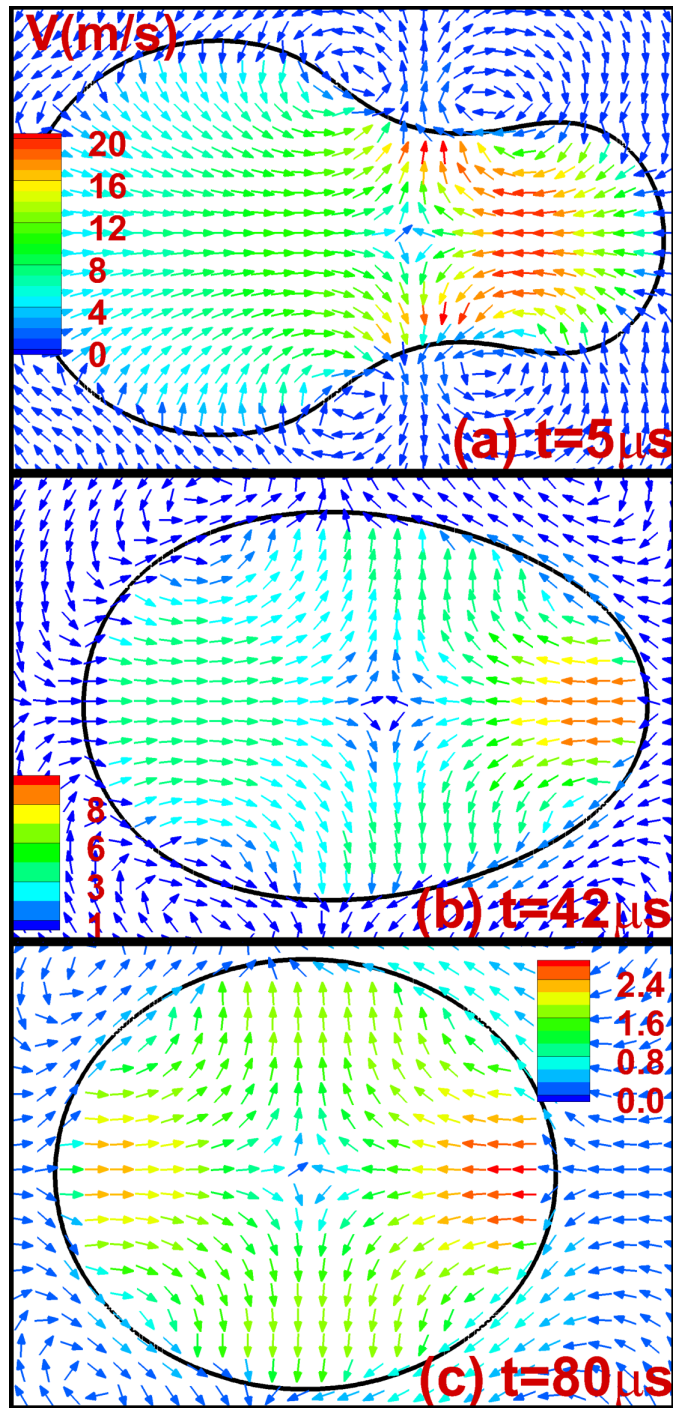
Figure 8: (Color online) Velocity vector fields at three representative time instants in the bubble coalescence for the case of $\gamma = 1.6$, $Oh = 3.3 \times 10^{-2}$: (a)$t = 5\mu s$, (b)$t = 42\mu s$, and (c)$t = 80\mu s$. The legend indicates the velocity magnitude ($V = \sqrt{u_x^2 + u_y^2}$). The uniform vector arrows only show the flow direction.
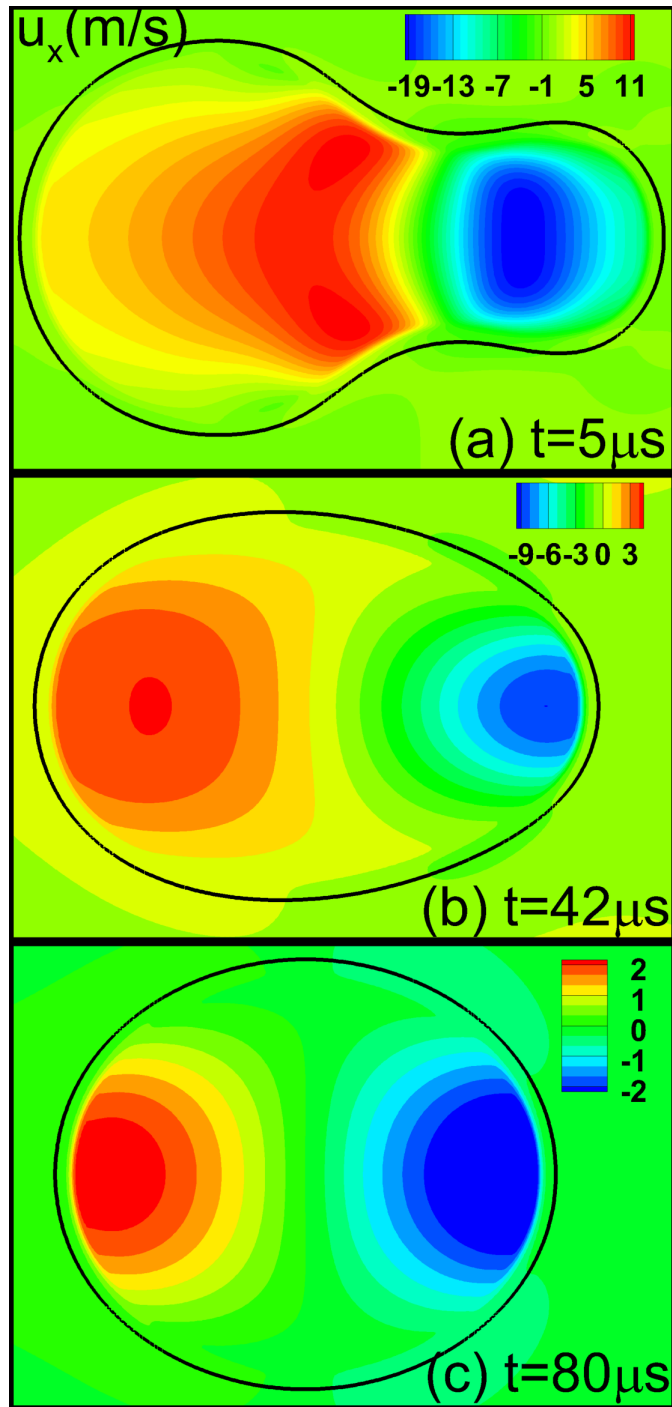
Figure 9: (Color online) Horizontal-component velocity (u_x) fields at three representative time instants in the bubble coalescence for the case of $\gamma = 1.6$, $Oh = 3.3 \times 10^{-2}$: (a)$t = 5\mu s$, (b)$t = 42\mu s$, and (c)$t = 80\mu s$. The legend indicates the magnitude and direction of u_x. Red means flowing to right and blue means to left.
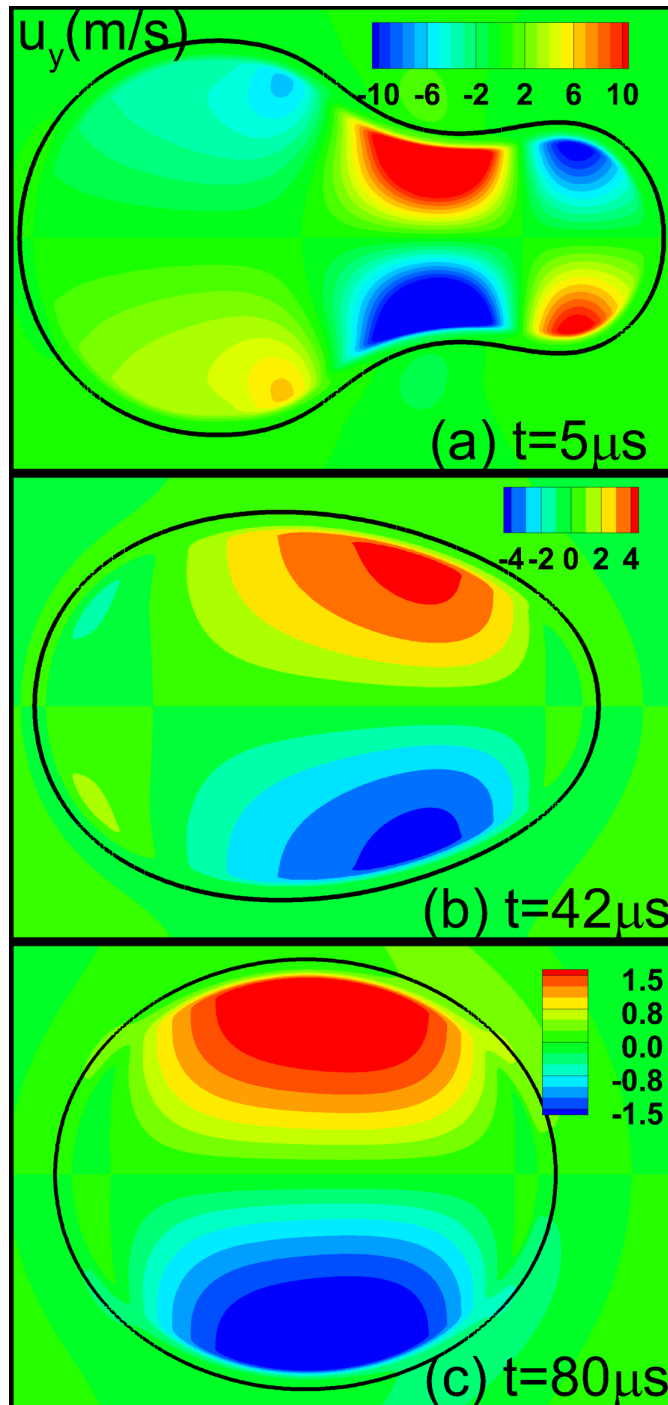
Figure 10: (Color online) Vertical-component velocity (u_y) fields at three representative time instants in the bubble coalescence for the case of $\gamma = 1.6$, $Oh = 3.3 \times 10^{-2}$: (a)$t = 5\mu s$, (b)$t = 42\mu s$, and (c)$t = 80\mu s$. The legend indicates the magnitude and direction of u_y. Red means flowing down and blue means up.
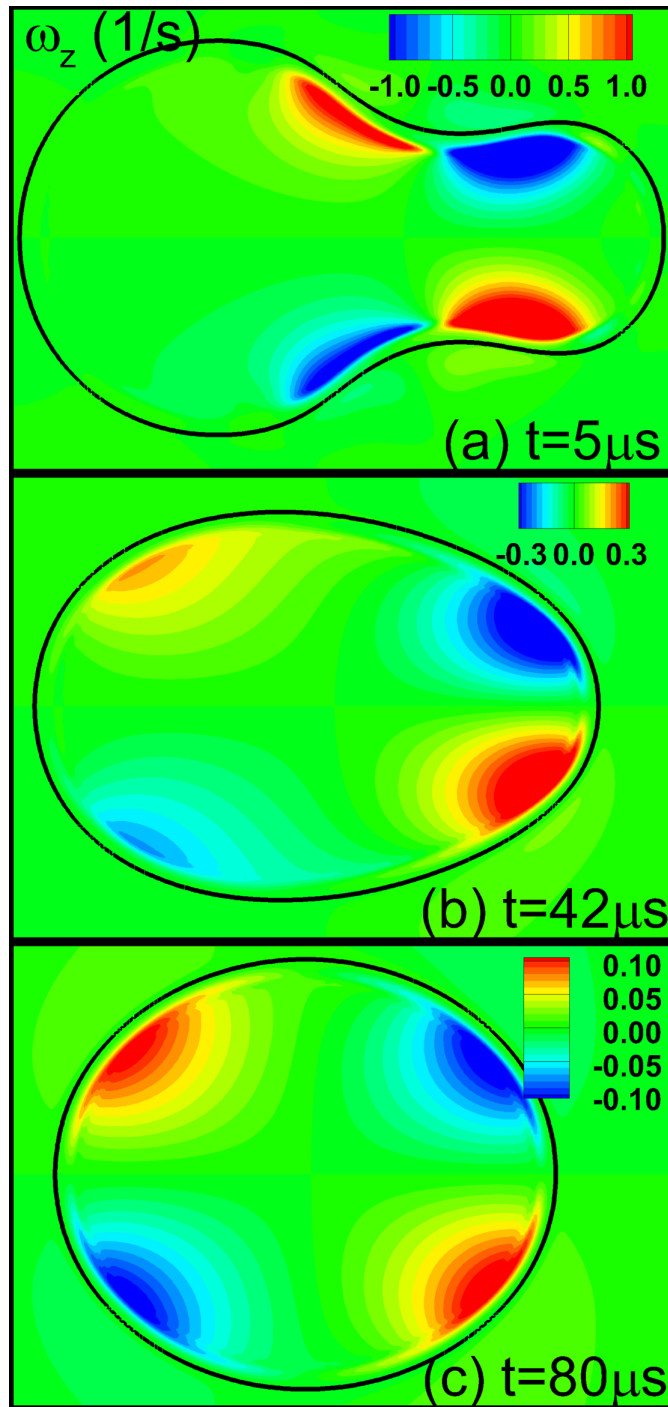
Figure 11: (Color online) Vorticity ($\omega = \partial u_y / \partial x - \partial u_x / \partial y$) fields at three representative time instants in the bubble coalescence for the case of $\gamma = 1.6$, $Oh = 3.3 \times 10^{-2}$:(a)$t = 5\mu s$, (b)$t = 42\mu s$, and (c)$t = 80\mu s$. The legend indicates the magnitude and direction of ω. Red means anti-clockwise rotation and blue means clockwise rotation.